CEAS Space Journal
https://doi.org/10.1007/s12567-024-00550-2

ORIGINAL PAPER

Satellite design optimization for differential lift and drag applications

Claudia Marianowski[1] · Constantin Traub[1] · Marcel Pfeiffer[1] · Julian Beyer[1] · Stefanos Fasoulas[1]

Received: 20 November 2023 / Revised: 29 February 2024 / Accepted: 26 March 2024

Abstract

Utilizing differential atmospheric forces in the very low earth orbits (VLEO) regime for the control of the relative motion within a satellite formation is a promising option as any thrusting device has significant impact on system design due to the limited weight and size restrictions of small satellites. One possible approach to increase the available accelerations caused by the atmosphere is to reduce the mass of the respective satellites as well as to increase the available surface area. However, satellites of these characteristics suffer from rapid orbital decay and consequently have a reduced service lifetime. Therefore, achieving higher control forces is in contradiction to achieving a minimum orbital decay of the satellites, which currently represents one of the biggest challenges in the VLEO regime. In this article, the geometry of a given reference satellite, a 3UCubeSat, is optimized under the consideration of different surface material properties for differential lift and drag control applications while simultaneously ensuring a sustained VLEO operation. It is worth noting that both the consideration of sustainability as well as the optimization with regard to differential lift are new in literature. It was shown that the advantageous geometries strongly depend on the type of gas–surface interaction and thus, two different final designs, one for each extreme type, are presented. In both cases, improvements in all relevant parameters could be achieved solely via geometry adaptions.

Keywords VLEO · Satellite aerodynamics · Satellite shape optimization · Differential drag and lift

1 Introduction

In the recent past, interest in operating satellites at much lower altitudes than before, in the so-called VLEO regime (i.e., the entirety of orbits with a mean altitude < 450 km [1]), has increased due to a variety of advantages, which have been summarized by Crisp et al. [1]. Similarly, the application of distributed satellite systems, which commonly are made up of several small satellites working together to achieve a shared goal, is nowadays prevalent [2]. Due to their stringent volume and mass limitations, alternative solutions to the conventional propulsion methods to exert control forces are of great interest. In the VLEO regime, the use of the atmospheric forces from the prevailing residual atmosphere represents a promising solution.

The methodology of differential drag, i.e., intentionally applying differences in the atmospheric drag forces of two or more spacecraft flying in formation to generate differential forces between them, was introduced by Leonard et al. [3] in 1987. Due to its promising benefits, differential drag methods have been investigated by different research groups worldwide (see Refs. [4–9]) and have regularly been demonstrated in-orbit [10–13]. However, the control authority of differential drag is primarily constrained to in-plane motion. The drag force in the out-of-plane direction, particularly for inclinations $i \neq 0°$ due to the co-rotating atmosphere, has been demonstrated to be two orders of magnitude smaller, even for highly inclined orbits [14], rendering it ineffective for meaningful control authority. In response, Horsley et al. [15] introduced the concept of utilizing differential lift as a means to control out-of-plane motion in 2011. In the following, an active exploitation of aerodynamic lift has been studied for the relative motion control (see e.g., Refs. [16–18]), or to maintain the sun-synchronous inclination despite aerodynamic drag [19]. Additionally, Virgili-Llop et al. [19] assessed the achievable lift to drag ratios for different satellite surface properties.

Claudia Marianowski
marianowskic@irs.uni-stuttgart.de

Constantin Traub
ctraub@irs.uni-stuttgart.de

[1] Institute of Space Systems, University of Stuttgart, Pfaffenwaldring 29, 70569 Stuttgart, Germany

At the Institute of Space Systems of the University of Stuttgart, this methodology has been actively researched since 2018 [20–23]. In the most recent publication, a planning tool for optimal three-dimensional formation flight maneuvers of satellites in VLEO using aerodynamic lift and drag via yaw angle deviations has been presented [22]. As in the VLEO regime the large levels of orbital decay represent the major challenge to be overcome for a sustained operation to become reality, the planned trajectory is optimal in a sense that the overall decay during the maneuver is minimized. Thereby, the remaining lifetime of the satellites is maximized, and the practicability and sustainability of the methodology significantly increased. Additionally, applying yaw angle deviations allows the simultaneous control of the in- and out-of-plane relative motion via differential lift and drag. However, it should be noted that aerodynamic force control methods are unlikely to be used for time-critical maneuvers due to the relatively small control forces.

Throughout the work of Traub et al. [22] conventional 3UCubeSats augmented with two solar panels have been assessed. In parallel efforts, optimized shapes for VLEO satellites targeting a minimization of the atmospheric drag force and thus extension of operational lifetime have been developed. Thereby, the satellite geometry has been optimized via a novel 2D profile optimization tool [24], which additionally allows the consideration of tapered tail geometries to further decrease the drag force as investigated by Walsh and Berthoud [25]. It was shown that the optimized satellite geometries offer pure passive lifetime extensions of up to 46 % compared to a GOCE like reference body.

In this article, which builds upon said contributions, optimal satellite designs for differential lift and drag applications are presented based on the current state-of-knowledge in terms of satellite aerodynamics. To the best of the authors' knowledge, such efforts have never been discussed in the literature. The article elaborates how the research objective leads to conflicting requirements, which need to be prioritized accordingly to arrive at an overall optimal design. All optimization steps are presented in detail and the corresponding considerations are discussed. While this is performed on the specific example of a 3UCubeSat, general conclusions are derived based on the results. In future efforts, it is foreseen to combine the optimal maneuver planning and the optimal satellite designs, which would represent a more holistic optimization approach.

The article is structured as follows: the necessary fundamentals are briefly presented in Sect. 2 before in Sect. 3, all relevant parameters and constraints as well as the applied optimization steps are introduced. The design optimization for diffuse reflection is conducted in Sect. 4, and the similar process for specular reflection can be found in Sect. 5. Finally, the results obtained are used to draw general conclusions in Sect. 6 before a summary and an outlook is given in Sect. 7.

2 Satellite aerodynamics

2.1 Fundamentals

The aerodynamic force acting on a satellite is the result of the interchange of momentum between the atmospheric particles and the satellite surface. The overall specific aerodynamic force

$$\boldsymbol{f}_{\mathrm{A}} = \boldsymbol{f}_{\mathrm{D}} + \boldsymbol{f}_{\mathrm{L}} \tag{1}$$

can thereby be separated into a specific drag force $\boldsymbol{f}_{\mathrm{D}}$, acting anti-parallel to the relative velocity vector, as well as a specific lift force $\boldsymbol{f}_{\mathrm{L}}$, defined as any atmospheric force perpendicular to drag. For a satellite of mass m, the specific drag force $\boldsymbol{f}_{\mathrm{D}}$ and lift forces $\boldsymbol{f}_{\mathrm{L}}$ can be calculated as shown in Eq. 2 and Eq. 3:

$$\boldsymbol{f}_{\mathrm{D}} = -\frac{1}{2} \cdot \rho \cdot \frac{C_{\mathrm{D}} \cdot A_{\mathrm{ref}}}{m} \cdot |\boldsymbol{v}_{\mathrm{rel}}|^2 \cdot \frac{\boldsymbol{v}_{\mathrm{rel}}}{|\boldsymbol{v}_{\mathrm{rel}}|}, \tag{2}$$

$$\boldsymbol{f}_{\mathrm{L}} = -\frac{1}{2} \cdot \rho \cdot \frac{C_{\mathrm{L}} \cdot A_{\mathrm{ref}}}{m} \cdot |\boldsymbol{v}_{\mathrm{rel}}|^2 \cdot \hat{\boldsymbol{u}}_{\mathrm{L}}, \tag{3}$$

where ρ is the atmospheric density, C_{D} the drag coefficient, C_{L} the lift coefficient, A_{ref} is the reference area,[1] $\boldsymbol{v}_{\mathrm{rel}}$ is the relative velocity to the local atmosphere and $\hat{\boldsymbol{u}}_{\mathrm{L}}$ is the effective lift direction:

$$\hat{\boldsymbol{u}}_{\mathrm{L}} = \frac{(\boldsymbol{v}_{\mathrm{rel}} \times \hat{\boldsymbol{n}}) \times \boldsymbol{v}_{\mathrm{rel}}}{|(\boldsymbol{v}_{\mathrm{rel}} \times \hat{\boldsymbol{n}}) \times \boldsymbol{v}_{\mathrm{rel}}|}, \tag{4}$$

which is dependent on the surface normal vector $\hat{\boldsymbol{n}}$ of the surface under consideration.

As atmospheric drag consistently dissipates energy from the satellite, the semi-major axis a of a satellite gradually decreases until re-entry occurs. An estimation of the remaining lifetime of a satellite in a circular orbit can be made via [26]:

$$t_{\mathrm{l}} = \frac{\beta \cdot H_0}{\rho_0 \cdot \sqrt{\mu_{\mathrm{E}} \cdot a}} \cdot \left(1 - \exp\left(-\frac{h_0}{H_0}\right) \cdot \left(1 + \frac{h_0}{2a}\right)\right). \tag{5}$$

Here, t_{l} is the passive lifetime of a satellite at a base altitude of h_0 for a given ballistic coefficient β defined as:

---

[1] Throughout this article defined as the projected area of the satellite perpendicular to the flow.

Table 1 Parameters for the piecewise exponential density model [26]

h [km]	h_0 [km]	ρ_0 [kg m^{-3}]	H_0 [km]
250–300	250	7.25×10^{-11}	45.55
300–350	300	2.42×10^{-11}	53.63
350–400	350	9.52×10^{-12}	53.30
400–450	400	3.73×10^{-12}	58.52

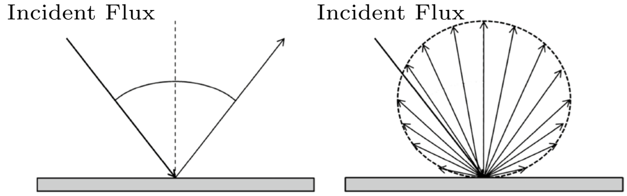

Fig. 1 Specular reflection (left) and diffuse reflection (right) [29]

$$\beta = \frac{m}{C_D \cdot A_{ref}} \tag{6}$$

In Eq. 5, H_0 is the atmospheric scale height and ρ_0 the respective density (see Table 1). μ_E is the Earth's gravitational parameter and $a = h_0 + R_E$ the semi-major axis with R_E being the Earth's radius. Although Eq. 5 only allows for an estimation of the passive satellite lifetime under the assumption of a spherical atmosphere and neglecting density fluctuations, it is well suited to assess the influence of satellite design variations (in analogy to the work of Hild et al. [24]).

2.2 Aerodynamic coefficients and gas–surface-interaction

In the VLEO regime, the atmosphere is so rarefied that the mean free path length exceeds the typical dimensions of a satellite. Consequently, the atmosphere is considered to be particulate in nature and the forces and torques acting on a spacecraft are the result of momentum and energy exchange between the incident gas particles and the external surfaces, commonly referred to as gas–surface-interaction (GSI). Two extreme cases of scattering mechanisms are differentiated (see Fig. 1); specular reflections, where the angle between surface and reflected particle is equal to the angle between surface and incoming particle, and diffuse reflections, with a particle reflection according to a probabilistic velocity and direction distribution. Throughout this article, Sentman's GSI model [27] was employed to describe the case of diffuse reflection, whereas the Cercignani-Lampis-Lord (CLL) model [28] is the model of choice for specular reflections. As input parameters, these models require so-called accommodation coefficients, which are introduced in the following section.

2.2.1 Accommodation coefficients

To mathematically describe the nature of the gas–surface interactions besides the two extreme cases, so-called accommodation coefficients are generally consulted. The thermal energy accommodation coefficient

$$\alpha_T = \frac{E_i - E_r}{E_i - E_w} \tag{7}$$

is a measure for the adaption of energy from the impinging particles E_i to the energy E_w, which the particles would have after reaching equilibrium with the satellite's wall temperature. E_r corresponds to the actual energy of the reflected particles. No thermal accommodation, i.e., $\alpha_T = 0.00$, describes the case of full specular reflection, whereas a complete thermal accommodation, i.e., $\alpha_T = 1.00$, corresponds to a diffuse reflection. Similarly, the momentum exchange between particle and surface is commonly described by the tangential momentum accommodation coefficient σ_t and the normal momentum accommodation coefficient σ_n as follows [28]:

$$\sigma_t = \frac{\tau_i - \tau_r}{\tau_i - \tau_w}, \tag{8}$$

$$\sigma_n = \frac{p_i - p_r}{p_i - p_w}. \tag{9}$$

Here, τ_i is the tangential momentum carried to the surface by the incident particle and τ_r is the tangential momentum carried away from the surface by the reflected particle. The tangential momentum carried away from the surface by a diffusely reflected particle after reaching thermal equilibrium with the wall is ascribed to τ_w and is per definition equal to zero as the mean path of re-emission is normal to the surface (see Fig. 1 right). The normal momentum carried to the surface by the incident particle and normal momentum carried away from the surface by the reflected particle are p_i and p_r respectively, and p_w is the normal momentum carried away from the surface by a diffusely reflected particle after reaching thermal equilibrium with the wall. The surface properties considered within this work can be found in section 3.1.2.

2.3 Satellite relative motion control via differential lift and drag

To adapt the design of a given satellite formation or to maintain it despite given perturbing sources, control forces need to be generated. In that respect, the method of differential

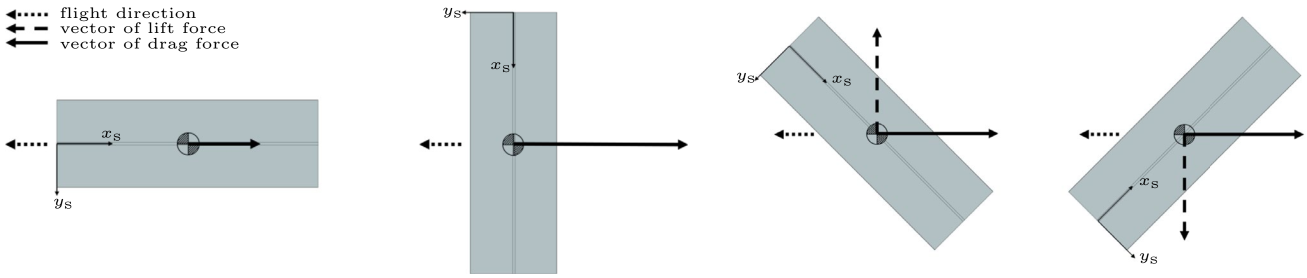

(a) Maximum differential drag $\delta \boldsymbol{f}_\mathrm{D}$ configuration.

(b) Maximum differential lift $\delta \boldsymbol{f}_\mathrm{L}$ configuration.

Fig. 2 Depiction of the relative satellite orientation of chief and deputy in the respective configurations

aerodynamic forces is generally understood as adjusting the relative motion of satellites via an intentionally created difference in the aerodynamic forces acting upon two satellites flying in formation (referred to as chief (subscript *C*) and deputy (subscript *D*) in the following) [20]

$$\delta \boldsymbol{f}_\mathrm{A} = \boldsymbol{f}_\mathrm{A,D} - \boldsymbol{f}_\mathrm{A,C}. \tag{10}$$

In accordance with Eq. 1, $\delta \boldsymbol{f}_\mathrm{A}$ can again be expressed as the sum of differential lift $\delta \boldsymbol{f}_\mathrm{L}$ and drag $\delta \boldsymbol{f}_\mathrm{D}$:

$$\delta \boldsymbol{f}_\mathrm{A} = \delta \boldsymbol{f}_\mathrm{L} + \delta \boldsymbol{f}_\mathrm{D}. \tag{11}$$

Whereas the methodology of differential drag $\delta \boldsymbol{f}_\mathrm{D}$ only allows to alter the relative motion within the orbital plane (in-plane relative motion), a simultaneous application of differential lift $\delta \boldsymbol{f}_\mathrm{L}$ and drag $\delta \boldsymbol{f}_\mathrm{D}$ enables three-dimensional formation flying maneuvers (out-of-plane adjustments via differential lift $\delta \boldsymbol{f}_\mathrm{L}$) [23]. Exemplary maximum differential drag (left) and lift (right) configurations for 3UCubeSats are displayed in Fig. 2.

2.3.1 Relevant configurations

Within this article, it is assumed that both satellites within the formation share the same design. Consequently, the following flight configurations, i.e., well defined orientations of the satellite with respect to the flow, are of particular interest throughout this article (see Fig. 2):

- **Nominal flight configuration:** Experiencing minimum drag $\boldsymbol{f}_\mathrm{D,min}$ (no lift),
- **Maximum drag configuration:** Experiencing maximum drag $\boldsymbol{f}_\mathrm{D,max}$,
- **Maximum lift configuration:** Experiencing maximum lift $\boldsymbol{f}_\mathrm{L,max}$.

As follows from Fig. 2, the norm of the maximum achievable differential drag force $\delta f_\mathrm{D,max}$ is the difference between the vector norm of the maximum $f_\mathrm{D,max}$ and the minimum drag $f_\mathrm{D,min}$ force. As lift by definition acts perpendicular to the drag force, the maximum norm of the differential lift force $\delta f_\mathrm{L,max}$ corresponds to two times the norm of the maximum achievable lift force $f_\mathrm{L,max}$, provided that the satellites are counter-rotated respectively (see Fig. 2a).

2.3.2 Prioritization

With respect to the configurations just defined, three separate optimization goals (OG) can be formulated to maximize the achievable differential lift $\delta f_\mathrm{L,max}$ and drag $\delta f_\mathrm{D,max}$ forces:

- **OG #1:** Decreasing $\boldsymbol{f}_\mathrm{D,min}$
- **OG #2:** Increasing $\boldsymbol{f}_\mathrm{D,max}$
- **OG #3:** Increasing $\boldsymbol{f}_\mathrm{L,max}$

Unfortunately, different satellite criteria are conducive to achieve the different optimization goals just formulated. Accordingly, this leads to conflicting requirements and an adequate prioritization is required for an overall optimal design. Furthermore, the absolute motion of the satellites and accordingly the environment in which the methodology is applied, namely the VLEO-range, cannot be ignored, as this could lead to extremely short satellite lifetimes and thus impractically short maneuver times. To achieve this goal, the practice of drag minimization via design optimization (decreasing $\boldsymbol{f}_\mathrm{D,min}$) from Hild et al. [24] should continue to be pursued.

Since orbital decay represents the biggest challenge to be overcome for a sustained satellite operation in VLEO to become reality, and as aerodynamic force control methods are unlikely the means of choice for time-critical maneuvers due to the comparatively low absolute values of specific forces, a reduction in orbital decay (i.e., a reduction of $\boldsymbol{f}_\mathrm{D,min}$ for a passive lifetime enhancement) is defined the main priority throughout this article (in line with the research goal of Traub [23]). As differential lift is shown to be inferior to drag [23], increasing the achievable lift forces $\boldsymbol{f}_\mathrm{L,max}$ to accordingly increase δf_L is set to be the second

Table 2 Atmospheric properties

Parameter	Unit	Value
T_i	K	1056.6
ρ	kg m^{-3}	9.15×10^{-12}
M	kg mol^{-1}	0.0174
v_{rel}	m s^{-1}	7,697.1
s	–	7.66
n_O	m^{-3}	2.64×10^{14}
n_{N2}	m^{-3}	4.18×10^{13}
n_{He}	m^{-3}	4.88×10^{12}
n_N	m^{-3}	4.44×10^{12}
n_{O2}	m^{-3}	1.09×10^{12}
n_H	m^{-3}	8.53×10^{10}
n_{Ar}	m^{-3}	8.63×10^{9}

priority within this article. Lastly, an increase in the achievable maximum drag force $f_{D,max}$ is targeted to maximize δf_D.

3 Methodology

Within this section, the chosen methodology to accomplish the defined goals alongside the utilized tools and optimization steps are elaborated.

3.1 Boundary conditions

3.1.1 Atmospheric conditions

The atmospheric conditions are defined constant within this article. Moderate space weather conditions (10.7 cm flux $F_{10.7}$ of 140 sfu and a geomagnetic activity index of $A_p = 15$) were used. The atmospheric properties, i.e., temperature of the impinging particle T_i, molecular mass M, molecular speed ratio s, and particle density n_i of species i, listed in Table 2 were obtained by averaging the output of the NRLMSISE-00 model [30] of one day per month of 2004 over the year for the chosen altitude of 350 km. The satellite's wall temperature is set to $T_w = 300$ K, in line with various studies presented in literature [31–33].

3.1.2 Reference satellite

All design variations are made with respect to a reference satellite to evaluate the influence of different satellite designs. Due to its universal applicability for various payloads and the size suitable for satellite formations, a 3UCubeSat with one panel each on the top and bottom is used as a reference satellite (see Fig. 3). For compliance with the commonly utilized CubeSats [34], the mass of the satellite is set to be 5 kg. The reference satellite has a maximum length l_{max} and height h_{max} of 0.3 m each as well as a main body volume V_{MB} of 0.003 m^3 with main body height h_{MB} and width of both 0.1 m. The width of the panel is equal to 0.003 m.

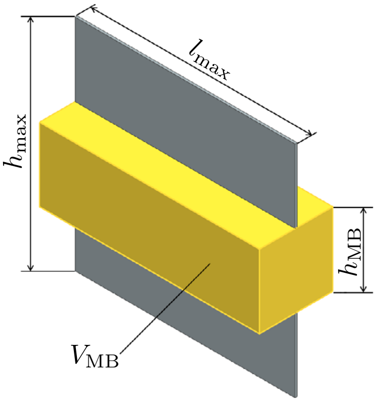

Fig. 3 Specifications of the reference satellite

The dependence of the atmospheric forces on the surface properties of the satellite is considered via different energy accommodation coefficients α_T and corresponding gas–surface-interaction models. The set of surface properties assessed is based on to the work of Traub et al. [21]: $\alpha_{T,1} = 1.00$ represents complete diffuse reflection with complete energy accommodation, $\alpha_{T,2} = 0.91$ is representative for traditional surface materials (derived via the SESAM model developed by Pilinski and Palo [35]) and $\alpha_{T,3} = 0.70$ represents improved material properties for diffusely reflecting materials. To ensure comparability, similar discrete steps are applied to the energy accommodation coefficient in case of specular reflection.

The relevant parameters of the reference satellite for the diffuse and specular case, which serve as a basis to quantify potential improvements of the optimized geometries within the later course of this article, are listed in Table 3.

Here, t_L and $f_{D,min}$ represent the lifetime and the specific drag force in the minimal drag configuration. $f_{D,max}$ is the specific drag force in the maximum drag configuration, $f_{L,max}$ the specific lift force in the maximum lift configuration, $f_{D,@L_{max}}$ the specific drag force in the maximum lift configuration, C_L/C_{Dmax} the lift to drag ratio in the maximum lift configuration. $\beta_{D,min}$ is the minimum ballistic (drag) coefficient, $\beta_{D,max}$ the maximum ballistic (drag) coefficient and $\beta_{D,@L_{max}}$ the ballistic (drag) coefficient in the maximum lift configuration. Finally, δf_D and δf_L are the maximum achievable differential drag and lift forces.

Table 3 Results for the reference design (3UCubeSat) for diffuse reflection ($\alpha_T = 1.00$) and specular reflection ($\alpha_T = 0.00$)

Parameter	Unit	Diffuse	Specular	Variation w.r.t diffuse %
t_L	d	157.09	142.40	− 9.35
$f_{D,\min}$	m s^{-2}	2.18×10^{-6}	2.38×10^{-6}	+ 10.34
$f_{D,\max}$	m s^{-2}	1.05×10^{-5}	1.96×10^{-5}	+ 87.38
$f_{L,\max}$	m s^{-2}	3.11×10^{-7}	6.90×10^{-6}	+ 2118.65
$f_{D,@L_{\max}}$	m s^{-2}	7.72×10^{-6}	1.16×10^{-5}	+ 49.85
$C_L/C_{D\max}$	–	0.04	0.60	+ 1380.57
δf_D	m s^{-2}	8.30×10^{-6}	1.72×10^{-5}	+ 107.39
δf_L	m s^{-2}	6.22×10^{-7}	1.38×10^{-5}	+ 2118.29
$\beta_{D,\min}$	kg m^{-2}	25.91	13.83	− 46.62
$\beta_{D,@L_{\max}}$	kg m^{-2}	35.10	23.42	− 33.28
$\beta_{D,\max}$	kg m^{-2}	125.64	113.89	− 9.35

3.1.3 Geometry constraints

To derive practical satellite designs, the following geometry constraints were defined:

- **Constant volume:** Main body volume remains constant.
- **Height and length limitations:** Maximum height and length of the reference satellite must not be exceeded.

Consequently, the mass of the satellite is constant ($m = 5$ kg = const.) and any variation in the residual force can be attributed to satellite design variations.

3.2 Tools and methods

Within this subsection, the open-source tools used to determine the aerodynamic coefficients [36, 37] as well as the 2D profile optimizer for satellite shapes targeting drag minimization [24] are introduced.

3.2.1 Determination of the aerodynamic coefficients

Since this study aims at an investigation of the influence of varying design parameters on the satellite's aerodynamic properties and therefore requires a multitude of calculations, a fast computation time is desired. Therefore, the MATLAB toolkit "ADBSat", which was developed at the University of Manchester [36], is the method of choice for the parameter study. ADBSat represents an advanced implementation of the widely used panel method, in which the geometry is represented as a set of flat triangular plates and the sum of their individual aerodynamic properties makes up the properties of the whole [36].

To examine promising designs in closer detail and to assess more complex effects such as gas–gas interactions or multiple reflections, the computationally intensive but proven Direct Simulation Monte Carlo (DSMC) method, which is available within the gas-kinetic simulation framework "PICLas", developed at the University of Stuttgart [37], is applied. For the PICLas simulations, the necessary variable hard sphere parameters for the species listed in Table 2 were taken from Bird [38].

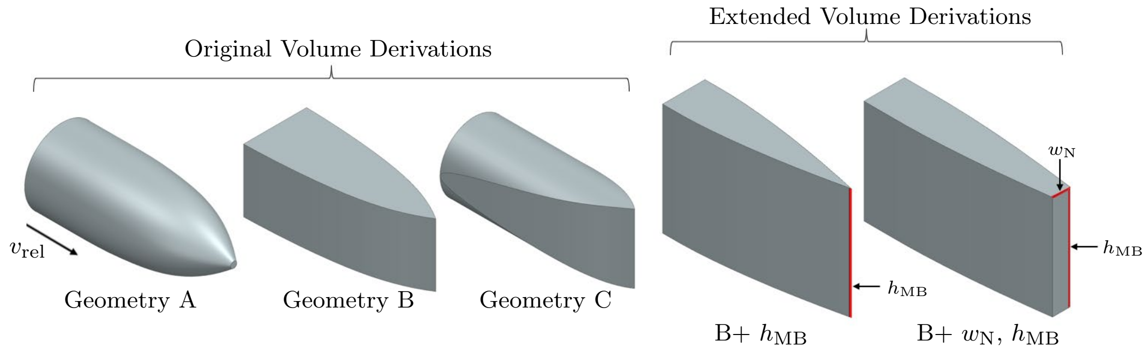

Fig. 4 Possible 3D volume derivations for the 2D optimization

3.2.2 2D profile optimizer

For optimizing the satellite body with respect to drag minimization and passive lifetime extension, the Matlab based 2D optimization tool developed by Hild et al. [24] is employed. It calculates an optimal 2D profile based on the respective GSI parameters. In addition, a maximum length and a constant volume condition are taken into consideration. For the latter, the type of 3D volume derivation needs to be defined prior to the optimization process. Three different volume derivation options are available (see Fig. 4): (A) rotation, (B) extrusion and (C) intersection of both. Additionally, a tapered tail profile

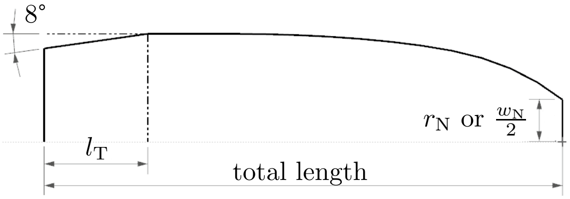

Fig. 5 Exemplary 2D profile with tapered tail according to Hild [39]

can be added (see Fig. 5). The tail length l_{T} must be given as input, whereas the frontal radius r_{N} for geometry option (A) or frontal width w_{N} for (B) and (C) result from the optimization process. Within this work, tail lengths of 0 % – 50 % of the total length were considered, and the respective l_{T} resulting in the least drag in minimum drag configuration were chosen.

To accomplish the research task of this article, the 2D profile optimization tool was extended as follows:

Additional geometry options: The extrude option (B) was modified to account for the following additional user inputs (see Fig. 4 (right)):

1. **Extrusion height h_{mb}**
2. **Nose width w_{N}**

Lift optimization: The 2D optimizer developed by Hild et al. [24] aims at optimizing the profile of a convex satellite such that the residual drag force is minimized. The fundamental theory to do so is thereby provided by Sentman [27]. Since only a 2D profile is optimized, two of the respective direction cosines become zero ($\eta, t = 0$). By adjusting the two remaining direction cosine according to the desired force direction of the lift force from the angle Θ_i to $\Theta_i + \frac{\pi}{2}$ (see Fig. 6) an optimization of a given profile with regard to increasing the lift force experienced by the profile is enabled.

3.3 Optimization steps

In this subsection, the optimization process, which is later on equally executed for diffuse (Sect. 4) and specular reflection (Sect. 5), is outlined.

3.3.1 Differential drag

To increase the control authority of differential drag, the goal is to minimize the residual drag force in the minimal drag configuration $f_{\mathrm{D,min}}$ and, vice versa, to maximize the residual drag force in the maximum drag configuration $f_{\mathrm{D,max}}$. Consequently, the optimization process for differential drag is divided into the following steps:

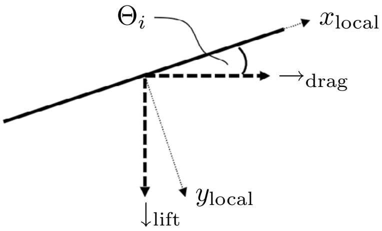

Fig. 6 Definition of the local axes of a surface element according to Hild [39]

Step 1a: The main body is optimized for minimum drag in the nominal flight configuration $f_{\mathrm{D,min}}$ utilizing the 2D profile optimization tool while maintaining the maximum length of 0.3 m and the main body volume of 0.003 m^3. Subsequently, the panel is optimized for minimal drag in the nominal flight configuration for a given extrusion height of 0.3 m.

Step 1b: The loss in the achievable maximum drag force $f_{\mathrm{D,max}}$ caused by the optimal profile needs to be best possibly be reduced. This can be achieved as follows:

- **Surface element alignment:** As the drag coefficient is maximal for surfaces perpendicular to the flow, the goal is to maximize the share of surface elements which fulfill this condition.
- **Multiple reflections:** A targeted insertion of sections in which multiple reflections are promoted increases the energy and momentum exchange per particle.

3.3.2 Differential lift

The goal for optimizing the design for differential lift consists solely of increasing $f_{\mathrm{L,max}}$. The process for optimizing the design for differential lift was divided into the following two steps:

Step 2a: For increasing the lift forces, an optimal profile is obtained via the 2D profile optimizer.

Step 2b: Reducing the areas which generate lift in the opposite direction represents an effective means to increase the overall lift force.

4 Design optimization - diffuse reflection

If not stated otherwise, the variations in the aerodynamic parameters are expressed with respect to the reference satellite assuming the same surface properties. For all ADBSat calculations performed within this section, Sentman's GSI model [27] was employed. The different design options derived and assessed are depicted in Figs. 9a–d.

4.1 Differential drag

In case of design optimization for differential drag applications, the influence of the satellite shape and of a tapered tail profile as well as of different surface structures has been analyzed.

4.1.1 Satellite shape and tail profile

As investigated by Hild et al. [24] and Walsh and Berthoud [25], a tapered tail profile on slender bodies represents an effective means for drag minimization as it serves to reduce the interaction between atmospheric particles and the satellite surfaces originally parallel to the flow. In the following, the effect of a tail geometry for the three different volume derivation options is investigated. Similarly, the influence of the design variation on the achievable maximum drag level is assessed. The influence of the tail length on the lifetime in nominal flight configuration, on the drag in maximum drag configuration as well as the resulting differential drag for different α_T is depicted in Fig. 10.

The optimum tail length depends on the volume derivation option and the surface properties. Whereas the geometry option (A) is advantageous for high values of α_T, the lifetime benefits for geometry options (B) and (C) increases with decreasing α_T. With respect to an increase in lifetime, geometry option (A) turned out to be the optimal choice. The respective tail length varied with the value of α_T: for $\alpha_T = 1.00$ and $\alpha_T = 0.91$ 23 % tail length and for $\alpha_T = 0.70$ 25 % led to the best results. However, as shown in Fig. 10a, geometry option (B) is advantageous in terms of the achievable drag forces in the maximum drag configuration due to its vertical side surfaces, which experience higher drag forces when oriented in maximum drag configuration and thereby perpendicular to the flow. Whereas for geometry option (A) an increase in lifetime of around 13% results, the reduction in the maximum achievable drag causes a reduction in the achievable differential drag with respect to the reference satellite (see Fig. 10b). Vice versa, the increase in lifetime with geometry option (B) is smaller than for (A) and (C), but due to the higher achievable maximum drag levels, an increase in differential drag compared to the reference satellite is possible. As increasing the lifetime was defined the top priority within this article, geometry option (A) will serve as the basis for the subsequent optimization steps.

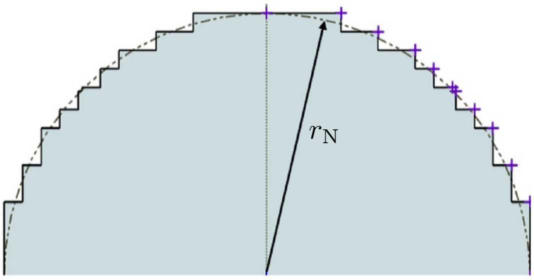

Fig. 7 Result of the *midpoint circle algorithm* for the rasterization of a given circular cross section

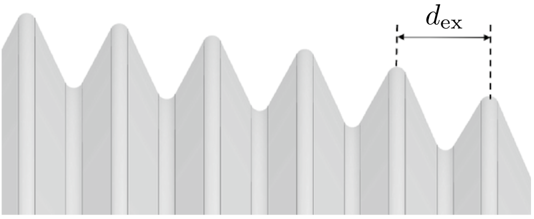

Fig. 8 Distance of the extrema d_{ex} of the overlayed *zigzag-curve* for the designs promoting multiple reflections

4.1.2 Surface structures

For geometry option (A), the maximum achievable drag is lower than for the reference satellite. By adding a rasterized cross section (see Fig. 7), the achievable drag in the maximum drag configuration can be increased as the area perpendicular to the flow in maximum drag configuration is increased. Meanwhile, the overall optimized profile shape in minimum drag configuration is maintained. To obtain the evaluated designs, the original frontal circular area, which was swept along the optimized profile, is rasterized via the so-called *midpoint circle algorithm*.[2] Two different raster step sizes, shown in Fig. 9a and b, have been applied. The step site of DiffOpt (Fine) and of DiffOpt (Coarse) is $r_N/14.3$ and $r_N/10$, respectively. Here, r_N is the radius of the frontal area, which results from the 2D profile optimization for geometry option (A) (see Fig. 5). In both cases, the constraint of a constant main body volume is met.

---

[2] The midpoint circle algorithm is an algorithm used for determining the points of a rasterized circle.

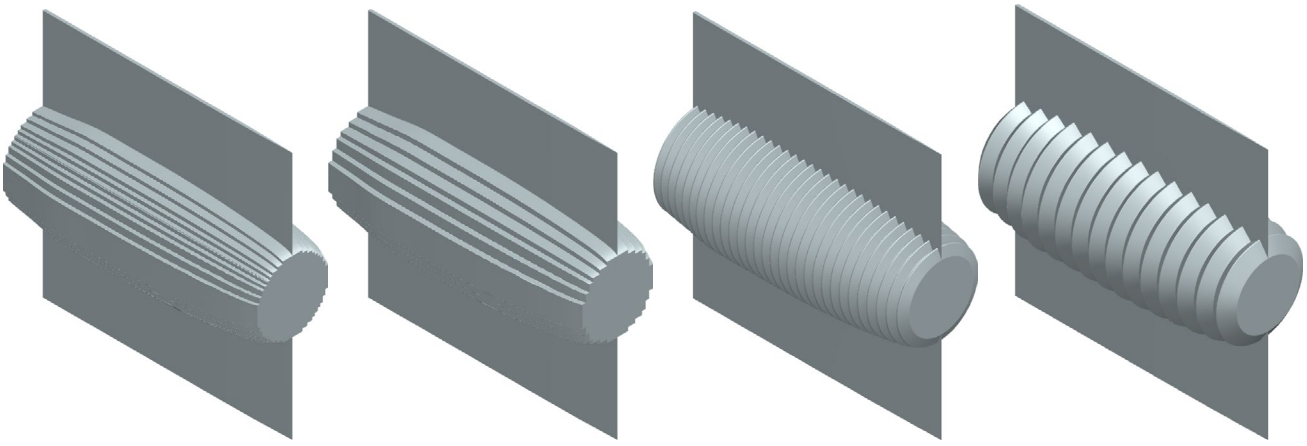

(a) DiffOpt (Fine) (b) DiffOpt (Coarse) (c) DiffMultiRef (Fine) (d) DiffMultiRef (Coarse)

Fig. 9 Selection of designs evaluated with PICLas and ADBSat in the case of diffuse reflection

The second option to increase the achievable maximum drag force is to integrate surface structures which promote multiple reflections. Therefore, the geometries shown in Fig. 9c and d, which are derived by overlaying the optimized profile for geometry option (A) with a *zigzag-curve* with an extrema distance d_{ex} of 5 mm (DiffMultiRef (Fine)) and 10 mm (DiffMultiRef (Coarse)), respectively. The definition of d_{ex} is indicated in Fig. 8.

The results, which have been derived via PICLas and are listed in Table 4, show that the additional surface area, which is now perpendicular to the flow in maximum drag configuration, represents a more effective means to increase the achievable maximum drag values than the designs promoting multiple reflections. The force distribution of the different designs compared to the reference satellite is shown in Fig. 11 for $\alpha_{\mathrm{T}} = 1.00$. The advantage of multiple reflections, however, is more than counteracted by the disadvantage resulting from decreased vertical surface areas, so that overall a reduction in the achievable drag results. Consequently, the idea of promoting multiple reflections will not be pursued further. Adding a rasterized cross section, on the other hand, demonstrably led to increased maximum drag values with similar levels in terms of lifetime benefits. Thus, this design is considered the most promising option.

4.2 Differential lift

Optimizing the profile of the satellite using the 2D profile optimizer for a given main body height led to a main body design resembling a 'wedge'. However, since in this case the side surface of the main body are not aligned with the panel (see Fig. 12a), the geometry could be further optimized by increasing the main body height to the original height of the panel to obtain one tall and slim wedge (see Fig. 12b). A major disadvantage of the resulting design is that it lacks practicability, as it contains a sharp nose geometry and hence poses difficulties concerning the payload accommodation. To address this, the effects of a frontal area (specified via a user-defined nose widths w_{N}) were investigated as well. For a given nose width, the overall frontal area increases with increasing main body height and so does the lift force pointing in the counterproductive direction. Hence, the greater the given nose width, the smaller the optimum main body height and the smaller the advantages in the achievable lift forces.

4.3 Differential lift and drag

For diffuse reflecting materials, the optimal designs for differential drag and for differential lift do not share many geometric characteristics. Based on the results obtained and with respect to the given prioritization, DiffOpt (Fine) represents the best possible trade-off, since the vertical side surfaces for increasing the maximum drag simultaneously have a positive effect on increasing the maximum lift force and an improvement in all critical parameters can be achieved. The respective flow-fields for the three relevant flight configurations for the reference satellite and design DiffOpt (Fine) are depicted in Figs. 13a-f. Due to the optimized profile, the area of increased density in Fig. 13b for $x < 0$ m is reduced accordingly. The reduction of the opposed lift force caused by the w.r.t. the satellite's system frontal area is visible in Fig. 13f, where the area of increased density preceding the frontal area of the recommended design is smaller compared to the reference satellite. The main results for the DiffOpt (Fine) design are listed in Table 5.

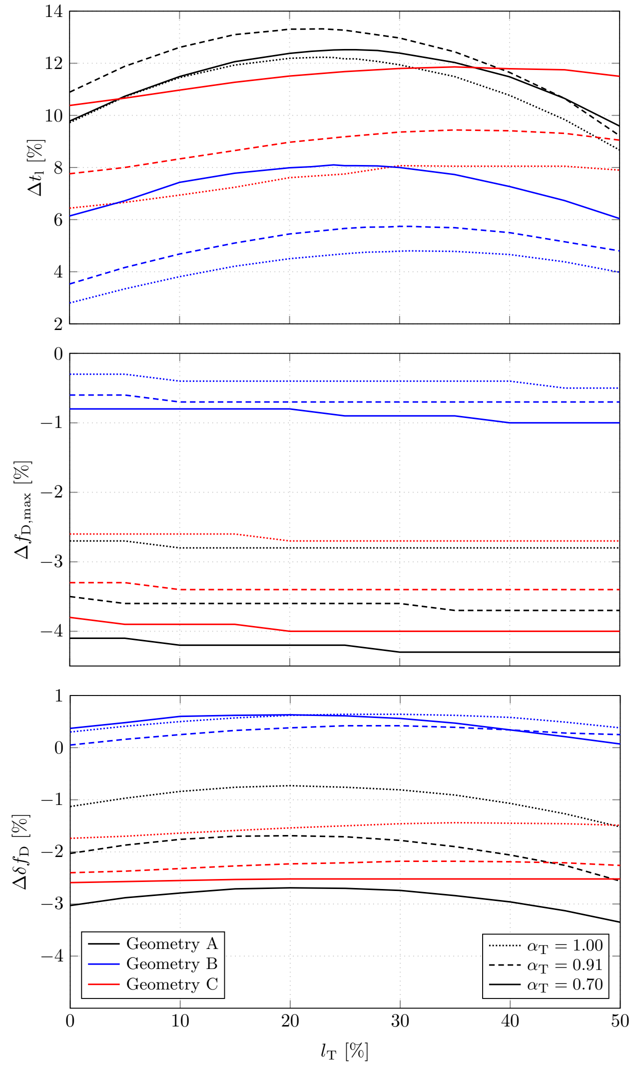

Fig. 10 Variation in lifetime t_{l} (top), maximum drag $f_{\mathrm{D,max}}$ (center), and differential drag δf_{D} (bottom) with changing base geometry (A, B or C), energy accommodation coefficient α_{T} and tail profile length l_{T} with respect to a 3UCubeSat (reference satellite)

5 Design optimization - specular reflection

For all ADBSat calculations performed within this section, the Cercignani-Lampis-Lord (CLL) model [29] is the GSI model of choice. The respective input parameters α_{n} and σ_{t} have been derived from α_{T} according to the conversions stated in Appendix B.

5.1 Differential drag

Within this section, the influence of general shape, the tail geometry, the main body height, and the frontal area on the experienced drag forces is assessed.

Table 4 Data for the tested designs with surface structures compared to the reference satellite, $\alpha_{\mathrm{T}} = 1.00$

Design	Δt_{l}	$\Delta f_{\mathrm{D,max}}$	$\Delta\delta f_{\mathrm{D}}$
DiffOpt (Fine)	+12.26 %	−0.32 %	+2.44 %
DiffOpt (Coarse)	+11.81 %	−0.31 %	+2.34 %
DiffMultiRef (Fine)	+3.27 %	−1.55 %	−1.13 %
DiffMultiRef (Coarse)	+0.35 %	−0.50 %	−0.54 %

5.1.1 Satellite shape and tail profile

In a first step, the influence of the volume derivation of the optimized 2D profile and the tail length is investigated. An overview of the lifetime in the nominal flight configuration for all three geometry derivation options (A), (B) and (C) and varying tail lengths is shown in Fig. 14.

For very low levels of energy accommodation, the geometry option (B) is the most advantageous option in terms of lifetime improvements. With increasing levels of accommodation, geometry option (C) becomes more beneficial. Additionally, Fig. 14 indicates that in this case, a tail geometry is counterproductive. The negative effect of the resulting increase in A_{ref} (see Eq. 2) counteracts the positive effect of a tapered tail.

5.1.2 Main body height

Subsequently, the influence of the main body height is analyzed. Figure 15 depicts the variation in lifetime in nominal flight configuration and in the resulting differential drag with changing main body height. For very low levels of energy accommodation, the overall lifetime, the experienced drag in maximum drag configuration and consequently also the differential drag force increases with the main body height. The optimized shape, referred to as SpecOpt (Theory), is depicted in Fig. 16a. A major disadvantage of this design is its lack in practicability (manufacture and payload accommodation).

A more practicable solution, referred to as SpecOpt (Pract) and depicted in Fig. 16b, can be obtained by including a frontal area (nose width w_{N}). The lifetime in nominal flight configuration and the resulting differential drag force for different nose geometries and different α_{T} is shown in Fig. 17. For a given w_{N}, a smaller main body height is advantageous with respect to the lifetime as any increase in h_{MB} simultaneously increases the frontal area. If the frontal area remains constant for different h_{MB}, i.e., a decreasing nose width w_{N} for increasing main body height h_{MB}, the influence of α_{n} and σ_{t} as well as the achievable improvement in lifetime and differential drag force decreases with increasing frontal area. Thus, the smallest possible main body height for a given nose width is desired. In any

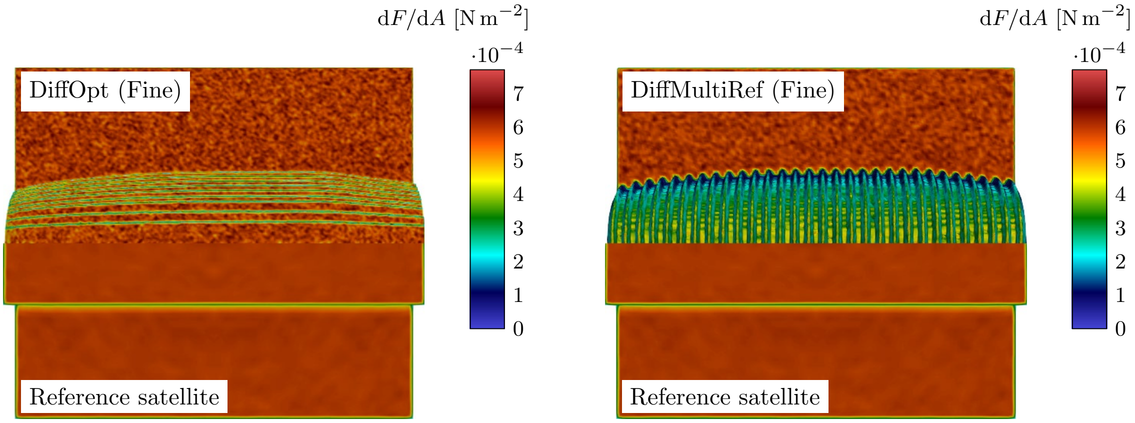

Fig. 11 Force distribution shown in head on view in maximum drag configuration for $\alpha_T = 1.00$

case, reducing the nose width as best as possible is desired as any frontal area leads to a significant loss in lifetime and consequently also reduces the achievable increase in differential drag compared to the reference satellite (see Figs. 15a and 17a).

5.2 Differential lift

For specular reflecting materials, the optimal profile corresponds to the design from Sect. 4.2. Figure 18 depicts the influence of the main body height for different levels of energy accommodation ($\alpha_T = [0.00;0.09;0.30]$). In analogy to the diffuse reflecting case, the optimal main body height is depending on the nose width. For increased lift forces, the frontal area should best possibly be reduced to mitigate lift forces in counterproductive directions.

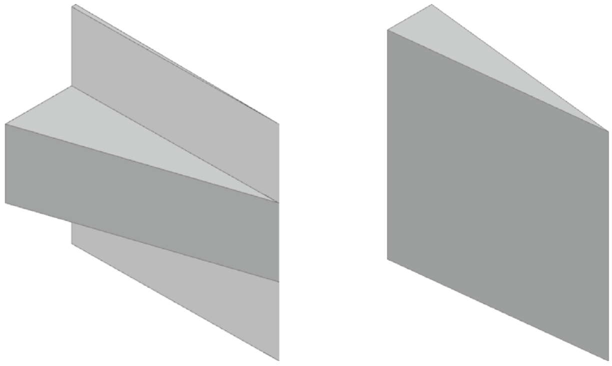

(a) Original $h_{\mathrm{MB}} = 0.10\,\mathrm{m}$ (b) $h_{\mathrm{MB}} = h_{\max}$

Fig. 12 Lift optimized designs with different main body heights h_{MB}

5.3 Differential lift and drag

For specular reflecting materials, the recommended designs for differential lift (resembling a tall and thin wedge) and differential drag (SpecOpt (Theory)) share many geometry characteristics. The major difference between the two designs is the slightly curved profile for the drag optimized shape. As SpecOpt (Theory) is beneficial in terms of lifetime (first priority) but comparable in case of the achievable lift force (second priority), design SpecOpt (Theory) would be well suited for an application of differential lift and drag. However, as already discussed, SpecOpt (Theory) represents a rather unrealistic design for a VLEO-satellite. Hence, a more practicable but less optimal solution including a minimum frontal area with a nose width of $w_N = 3$ cm is recommended in this case. To minimize the disadvantages in terms of lifetime, a minimal main body height is desired.

Table 5 Results for the recommended design DiffOpt (Fine) for diffuse reflection ($\alpha_T = 1.00$)

Parameter	Unit	Value	Variation w.r.t. reference
t_L	d	176.35	+12.26 %
$f_{D,\min}$	m s^{-2}	1.92×10^{-6}	−10.89 %
$f_{D,\max}$	m s^{-2}	1.04×10^{-5}	−0.29 %
$f_{L,\max}$	m s^{-2}	3.21×10^{-7}	+3.15 %
$f_{D,@L_{\max}}$	m s^{-2}	7.36×10^{-6}	−4.65 %
$C_L/C_{D\max}$	–	0.04	+8.18 %
δf_D	m s^{-2}	8.51×10^{-6}	+2.47 %
δf_L	m s^{-2}	6.42×10^{-7}	+3.13 %
$\beta_{D,\min}$	kg m^{-2}	25.99	+0.31 %
$\beta_{D,@L_{\max}}$	kg m^{-2}	36.82	+4.90 %
$\beta_{D,\max}$	kg m^{-2}	141.04	+12.26 %

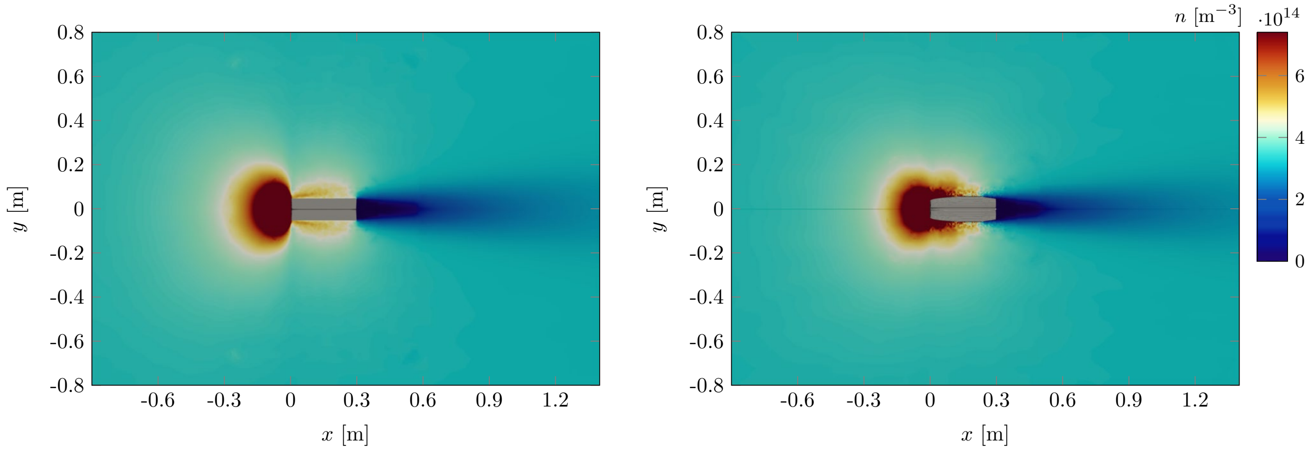

(a) Reference satellite - nominal flight

(b) DiffOpt (Fine) - nominal flight

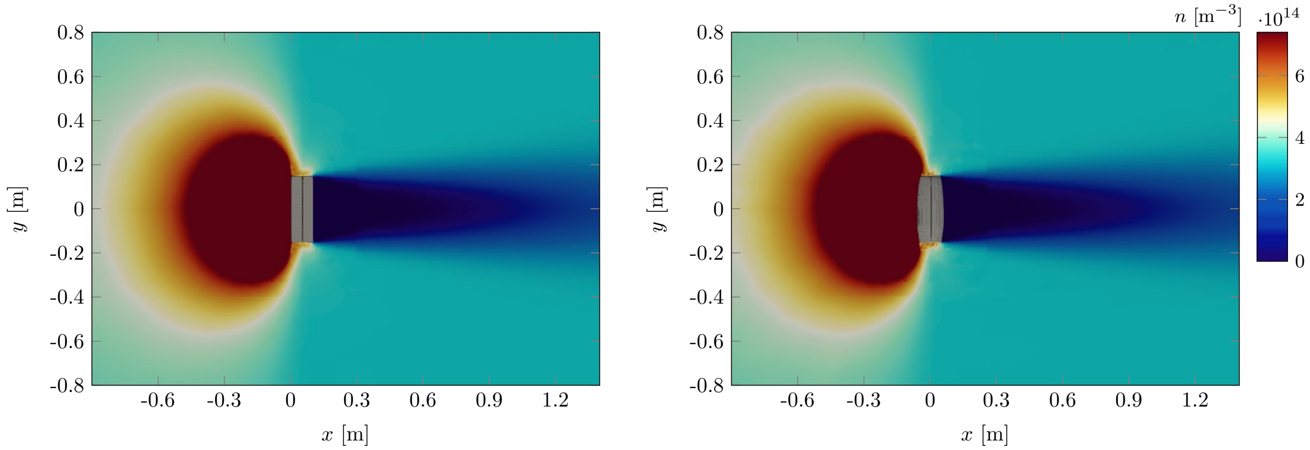

(c) Reference satellite - maximum drag

(d) DiffOpt (Fine) - maximum drag

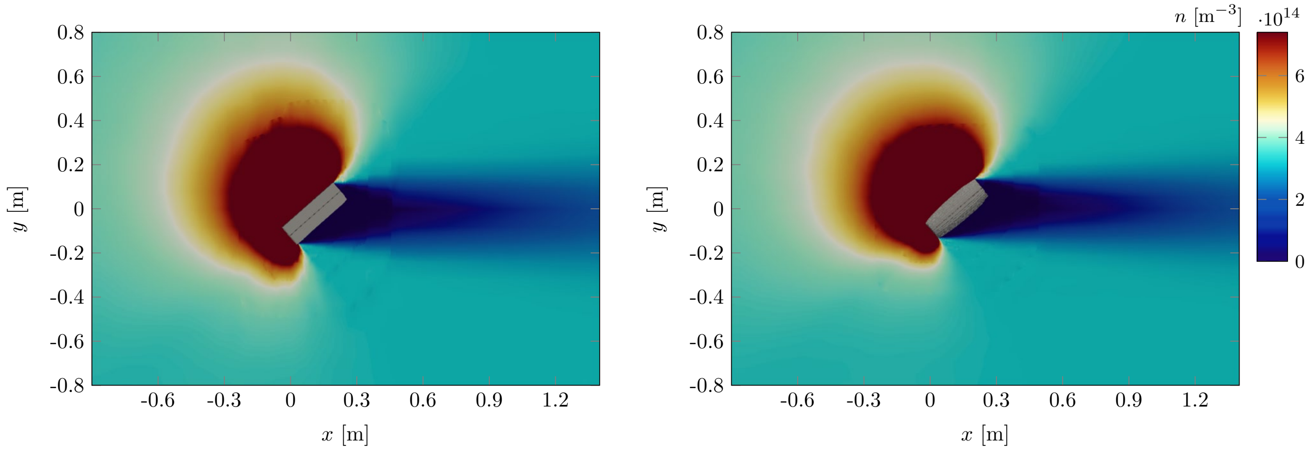

(e) Reference satellite - maximum lift

(f) DiffOpt (Fine) - maximum lift

Fig. 13 Simulated particle density n in the flow-field around the 3UCubeSat (reference satellite) (left) and the DiffOpt (Fine) (right) design for $\alpha_{\mathrm{T}} = 1.00$

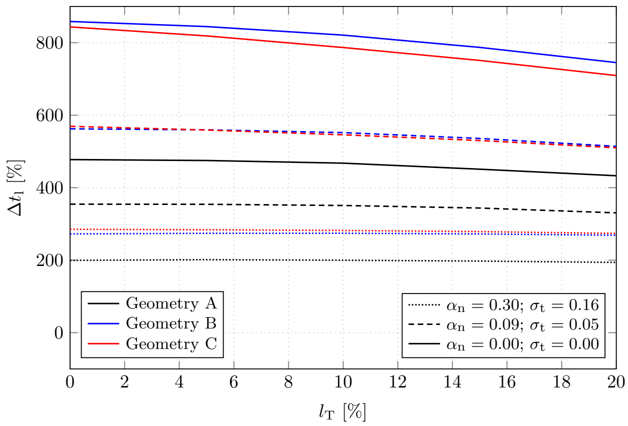

Fig. 14 Increase in lifetime Δt_L depending on general shape and tail length l_T w.r.t. the 3UCubeSat (reference satellite) with $\alpha_T = 1.00$

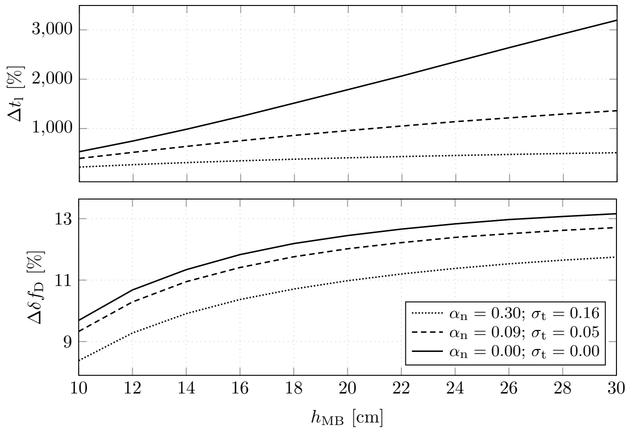

Fig. 15 Increase in lifetime Δt_L (top) and differential drag $\Delta\delta f_D$ (bottom) for the SpecOpt (Theory) design depending on the main body height h_{MB} with respect to the 3UCubeSat (reference satellite)

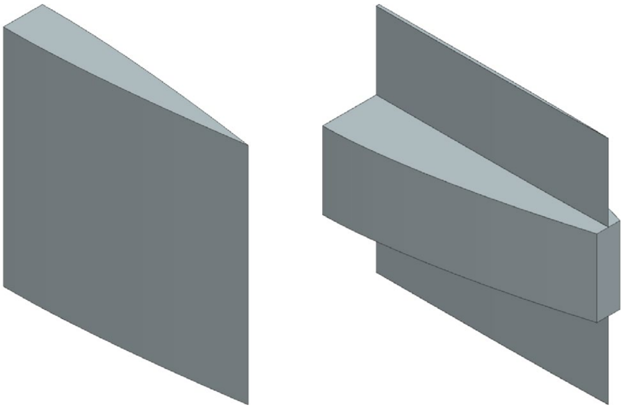

(a) SpecOpt (Theory)

(b) SpecOpt (Pract)

Fig. 16 Selection of designs evaluated with PICLas and ADBSat in the case of specular reflection

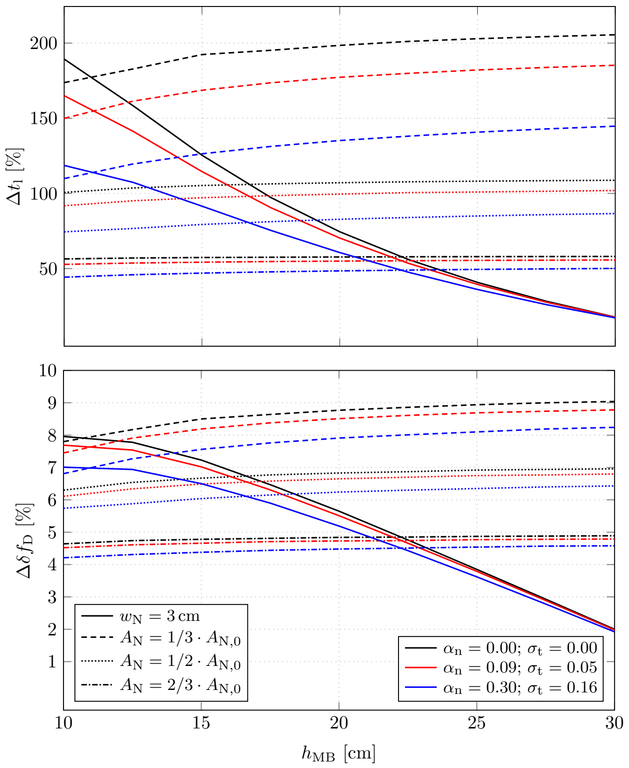

Fig. 17 Increase in lifetime Δt_L (top) and differential drag $\Delta\delta f_D$ (bottom) for the SpecOpt (Pract) design depending on the main body height for different frontal areas with respect to the 3UCubeSat (reference satellite)

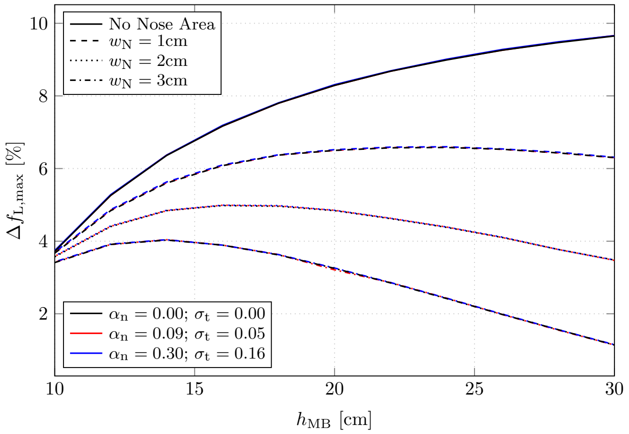

Fig. 18 Influence of the main body height h_{MB} and different nose widths for the on the achievable lift forces $\Delta f_{L,\max}$ for the SpecOpt (Theory) design with respect to the 3UCubeSat (reference satellite)

Consequently, it is set equal to the height of the reference satellite with $h_{MB} = 10$ cm. The resulting design, referred as SpecOpt (Pract), for $\alpha_T = 0.00$ is depicted in Fig. 16b.

The flow-fields for the reference satellite and SpecOpt (Pract) are compared in Fig. 19, and the main

Table 6 Results for the recommended design SpecOpt (Pract) for specular reflection ($\alpha_T = 0.00$)

Parameter	Unit	Value	Variation w.r.t diffuse %	Variation w.r.t specular %
t_L	d	427.14	+ 171.91	+ 199.96
$f_{D,min}$	m s^{-2}	7.93×10^{-7}	− 63.11	− 66.66
$f_{D,max}$	m s^{-2}	1.87×10^{-5}	+ 78.87	− 4.54
$f_{L,max}$	m s^{-2}	6.95×10^{-6}	+ 2133.12	+ 0.65
$f_{D,@L_{max}}$	m s^{-2}	1.06×10^{-5}	+ 37.81	− 8.04
$C_L/C_{D\max}$	-	0.65	+ 1520.48	+ 9.45
δf_D	m s^{-2}	1.79×10^{-5}	+ 115.83	+ 4.07
δf_L	m s^{-2}	1.39×10^{-5}	+ 2132.76	+ 0.65
$\beta_{D,min}$	kg m^{-2}	14.49	− 44.08	+ 4.77
$\beta_{D,@L_{max}}$	kg m^{-2}	25.49	− 27.38	+ 8.84
$\beta_{D,max}$	kg m^{-2}	341.61	+ 171.90%	+ 199.95

results for the SpecOpt (Pract) design are listed in Table 6. The detrimental effect of a frontal area on the lifetime can be seen in Fig. 19b, where the deflection of the impinging particles by 180° leads to an accumulation of particles ahead of the satellite. However, the reduction of the total frontal area compared to the reference results in an increase in lifetime. In Fig. 19d, the particles are reflected in a wider range with a downward shift due to the increased curvature of the main body's side surface. The overlapping region of particles reflected by the panels and particles reflected by the rearward part of the side surface can be seen in the range around $-0.5\ \text{m} < y < 0.3\ \text{m}$. In this case, the non-symmetrical deflection in the maximum drag configuration leads to a lift force, which is comparatively small, but nonetheless can build up to a considerable effect over time. As the main body's frontal surface area is smaller than the one of the reference satellite, the resulting lift forces increase (see Fig. 19f).

6 General conclusions and lessons learned

In this section, the results obtained for the specific example of a 3UCubeSat are used to derive general conclusions for satellite design optimizations of VLEO spacecraft which will be of use for the community for future optimization efforts of various satellite geometries.

6.1 Surface properties vs. design optimization

Throughout this article, the benefits of dedicated adjustments to the satellite design parameters have been assessed for both extreme types of reflection, i.e., diffuse and specular, as well as varying degrees of energy accommodation.

While benefits could be achieved through targeted design adjustments in any case, the results show consistently that a reduction of the level of degree of energy accommodation for a fully diffuse reflecting material represents the most powerful means to increase the available lift forces and is significantly more influential than any design variation efforts. Even more advantageous, however, are reflective material properties, which allow the entire aerodynamic behavior of the satellite, i.e., its minimum drag, differential lift and differential drag, to be selectively optimized. This is in line with the results of previous studies, e.g., from Hild et al. [24]. Thus, efforts aiming to identify and characterize enhanced surface materials with specular and/or quasi-specular reflection, as the recently ended DISCOVERER project [40], are critical to render the methodology a suitable option for future missions.

6.2 The tool of choice

As shown in Fig. 20 and discussed in Chapter A, the results obtained via ADBSat match well (maximum deviation of 4 %) with the results obtained via the considerably more powerful and computationally expensive tool PICLas. This is in line with the verification study of ADBSat by Sinpetru et al. [41]. Only in the cases for which multiple reflections are deliberately promoted, deviations up to 25 % result. Multiple reflections are an example of more complex behavior that cannot be represented with a tool based on the panel method. Using ADBSat, the calculation of the aerodynamic coefficients for one set of satellite geometry and orientation is within the subsecond range, whereas PICLas requires simulation times of up to 48 h depending on the available computational resources. On the other hand, the analysis of the flow fields (Figs. 13 and 19) and the resulting insights are only possible for the latter. Accordingly, the strategy of performing fast and preliminary analyses using the simplified tool (ADBSat) and subsequently recalculating critical cases using the more advanced tool (PICLas) is to be categorized as expedient.

6.3 Notes on the practicability of differential lift

Although differential lift is indispensable for the three-dimensional control of satellite formations, its practicability is currently limited due to a variety of reasons. Consequently, it is unlikely that this method will find frequent application in the immediate future [23]. However, a re-evaluation of the statement will likely turn out differently once specular or near-specular reflecting materials become available. Indeed, in this article it was shown that the aerodynamic characteristics of a state-of-the-art reference satellite can be modified such that improvements in lifetime by 172 %, in differential drag by 116 % and in differential lift by

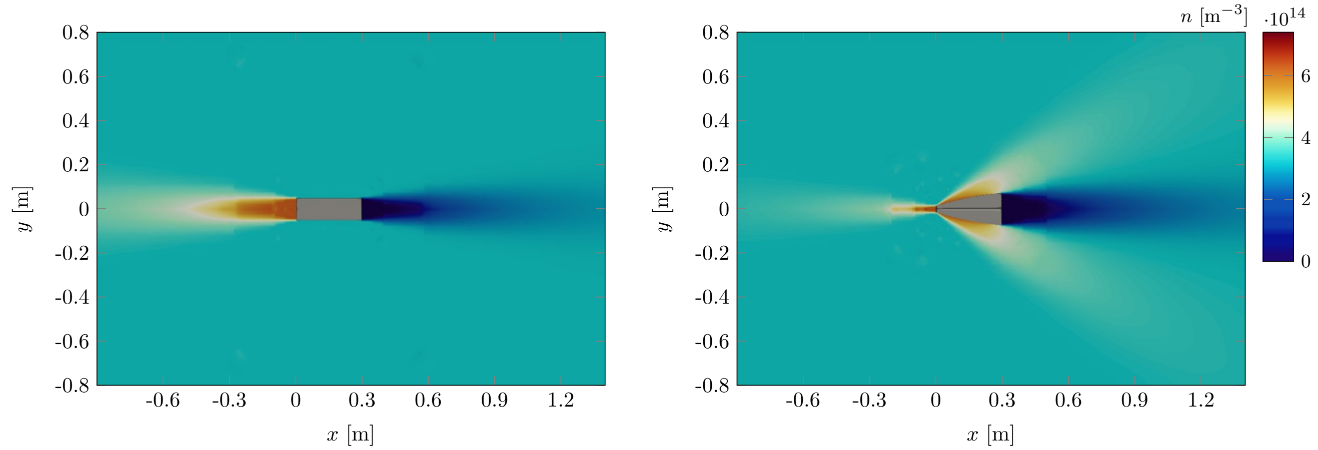

(a) Reference satellite - nominal flight

(b) SpecOpt (Pract) - nominal flight

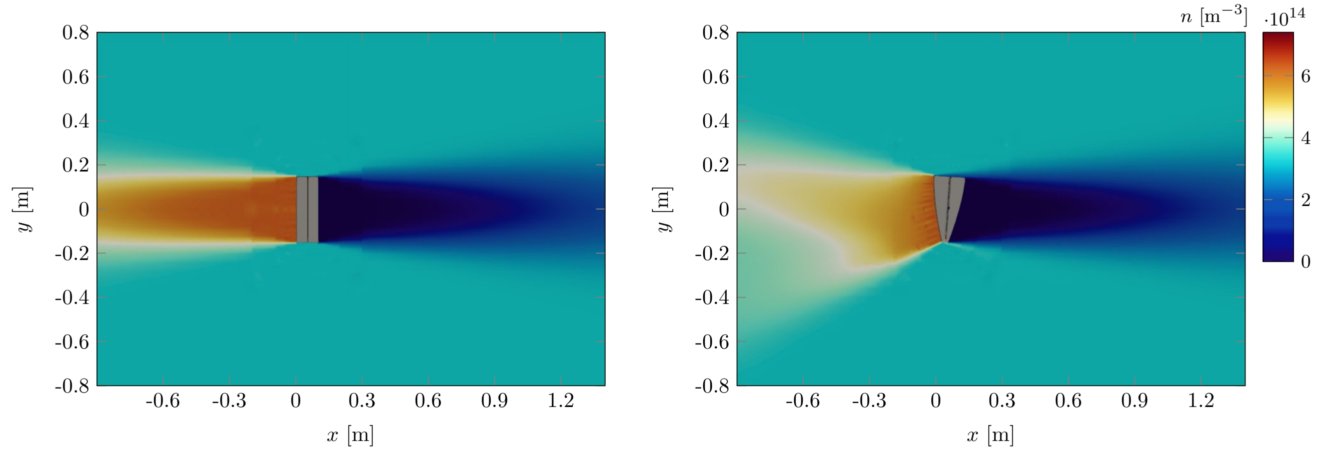

(c) Reference satellite - maximum drag

(d) SpecOpt (Pract) - maximum drag

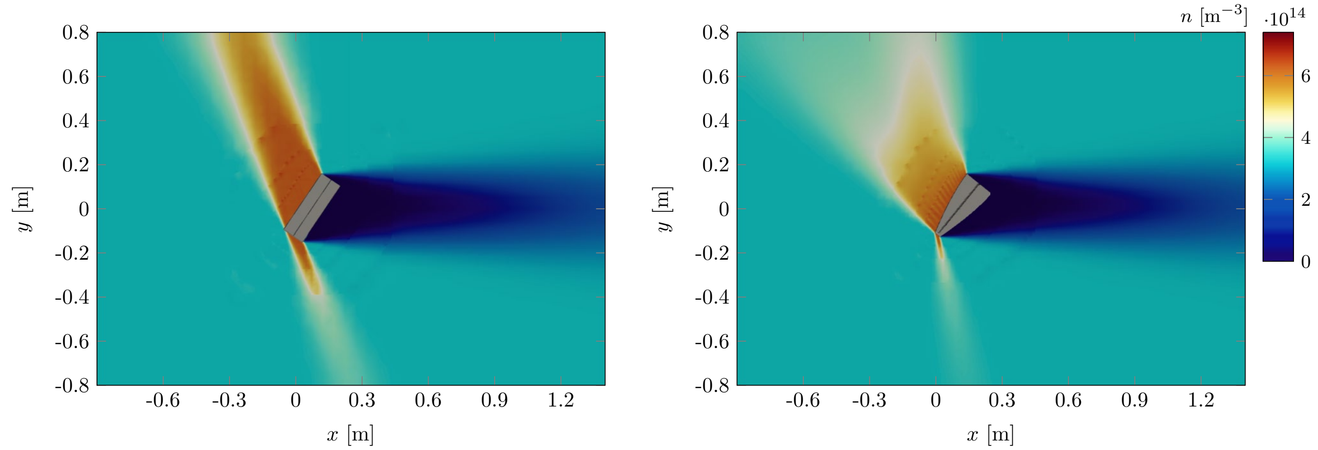

(e) Reference satellite - maximum lift

(f) SpecOpt (Pract) - maximum lift

Fig. 19 Simulated particle density n in the flow-field around the 3UCubeSat (reference satellite) (left) and the SpecOpt (Pract) design (right) for $\alpha_\mathrm{T} = 0.00$

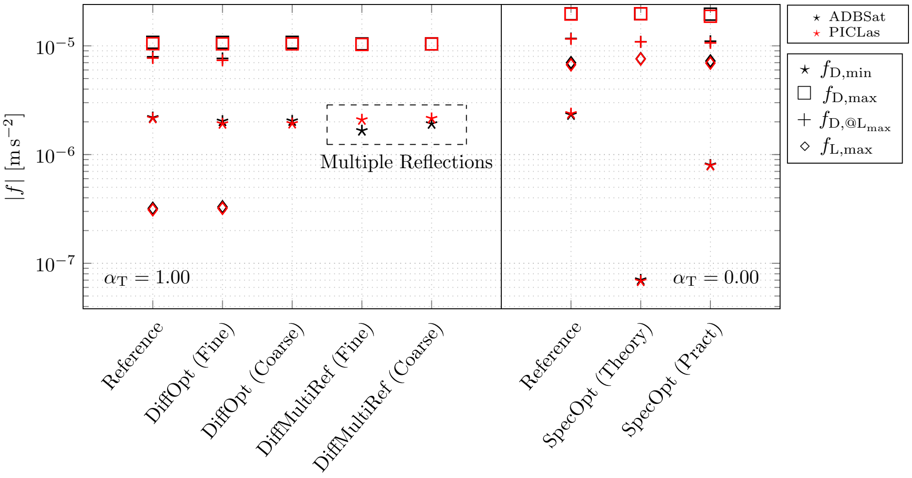

Fig. 20 Comparison of ADBSat and PICLas results

2133 % result. Should this actually be realizable in practice in the future, it would lead to completely new possibilities for propellant-less satellite out-of-plane relative motion control in VLEO.

7 Summary and outlook

In this article, the design of a reference satellite has been optimized with regard to a differential lift and drag application for both extreme cases of reflection (diffuse and specular). The research objective lead to conflicting requirements, which needed to be prioritized accordingly to arrive at an overall optimal design. While the design optimization focused on a specific 3UCubeSat example, general conclusions were drawn from the results. The influence of design variations was primarily evaluated using the "ADBSat" framework and the performance of the promising designs was verified using the DSMC code "PICLas".

For materials with diffuse reflection, the possibilities for optimization have proven to be limited. Nevertheless, design optimizations could be achieved. Even for the case of complete energy accommodation, the passive lifetime could be increased by 12 % while simultaneously increasing the available differential drag and lift forces by 2 % and 3 % respectively. Nevertheless, differential lift remains inferior to differential drag. Specularly reflective materials allow more scope for design optimization. Since the theoretical optimal design was of little practicability, a more practicable solution was presented. With respect to the reference satellite with a diffuse reflecting material, improvements of 172 % in lifetime, 116 % in differential drag and 2133 % in differential lift could be achieved. Should this actually be realizable in practice in the future, it would lead to completely new possibilities for propellant-less satellite out-of-plane relative motion control in VLEO. Research into advanced materials is therefore a top priority to enable the long-term operation of VLEO satellites and the control of the relative motion of satellites without propellant.

Table 7 Derived CLL input parameters

α_T [-]	α_n [-]	σ_t [-]
0	0	0
0.09	0.09	0.05
0.30	0.30	0.16

Since the optimized 3D designs presented and discussed throughout the article have been derived from optimal 2D profiles, a direct optimization of a 3D body is currently still pending. Additionally, an application of different surface properties within a single satellite design was not considered, which represents a possible continuation of this work. As an example: applying a diffusely reflecting frontal area (increased lifetime) and specular reflecting side surfaces (increased differential lift forces) represents an effective means for additional improvements. The data that support the findings of this study are available from the corresponding author upon reasonable request.

Appendix A comparison of ADBSat and PICLas results

In this section, the results obtained using ADBSat and PICLas for the recommended designs presented in the previous sections are compared. The results of the different designs are listed in Fig. 20.

In all except two cases, the results of ADBSat comply with the ones obtained using PICLas. A noticeable difference occurs for both DiffMultiRef designs for the minimum drag. Those designs, however, have deliberately been designed such that multiple reflections are promoted. Here, the minimum drag obtained using PICLas is 25 % higher for design DiffMultiRef (Fine) and 12 % higher for design DiffMultiRef (Coarse) than estimated with ADBSat.

Besides for these two designs, the maximum deviation between the values predicted by both tools is 4 %.

Appendix B Parameter conversions

For the application of the CLL model in ADBSat, the normal energy accommodation coefficient α_n and the tangential momentum accommodation coefficient σ_t are required and therefore are derived from the given α_T. The following derivation is based on transformations of Sentman's equation by Hild [39] and the consideration of a 2D profile.

Since the kinetic energy $E = \frac{1}{2}mv^2$ is proportional to the squared momentum $I^2 = m^2v^2$ under the assumption of constant mass, Eq. 7 can be also expressed as

$$\alpha_\mathrm{T} = \frac{I_\mathrm{i}^2 - I_\mathrm{r}^2}{I_\mathrm{i}^2 - I_\mathrm{w}^2}, \tag{B1}$$

with the momentum I consisting of its normal and tangential components p and τ

$$I^2 = p^2 + \tau^2. \tag{B2}$$

The normal and tangential energy accommodation coefficient α_n and α_t hence can be defined as

$$\alpha_\mathrm{n} = \frac{p_\mathrm{i}^2 - p_\mathrm{r}^2}{p_\mathrm{i}^2 - p_\mathrm{w}^2}, \tag{B3}$$

$$\alpha_\mathrm{t} = \frac{\tau_\mathrm{i}^2 - \tau_\mathrm{r}^2}{\tau_\mathrm{i}^2 - \tau_\mathrm{w}^2}. \tag{B4}$$

The parameter τ_i and p_i as properties of the impinging particle depend on the properties of the atmosphere and are proportional to the following terms [39]:

$$\tau_\mathrm{i} \propto \epsilon \left[\gamma(1 + \mathrm{erf}(\gamma s)) + \frac{1}{s\sqrt{\pi}} e^{-\gamma^2 s^2} \right], \tag{B5}$$

$$p_\mathrm{i} \propto \gamma \left[\gamma(1 + \mathrm{erf}(\gamma s)) + \frac{1}{s\sqrt{\pi}} e^{-\gamma^2 s^2} \right] + \frac{1}{2s^2}(1 + \mathrm{erf}(\gamma s)). \tag{B6}$$

τ_w is per definition equal to zero, and the normal momentum p_w carried away after reaching thermal equilibrium with the wall is proportional to

$$p_\mathrm{w} \propto \frac{1}{2}\sqrt{\frac{T_\mathrm{w}}{T_\mathrm{i}}} \cdot \left[\frac{\gamma\sqrt{\pi}}{s}(1 + \mathrm{erf}(\gamma s)) + \frac{1}{s^2} e^{-\gamma^2 s^2} \right], \tag{B7}$$

where T_w is the wall temperature of the satellite and T_i is the temperature of the incident particles [39]. Finally, the momentum components of the reflected particle have to be expressed. Therefore, Eq. B1 can be transformed into

$$I_\mathrm{r} = \sqrt{I_\mathrm{i}^2 - \alpha_\mathrm{T}(I_\mathrm{i}^2 - I_\mathrm{w}^2)}. \tag{B8}$$

Using Eq. B2 on I_i leads to

$$I_\mathrm{i} = \sqrt{p_\mathrm{i}^2 + \tau_\mathrm{i}^2}, \tag{B9}$$

which now can be used to express Eq. B8 as

$$I_\mathrm{r} = \sqrt{p_\mathrm{i}^2 + \tau_\mathrm{i}^2 - \alpha_\mathrm{T}(p_\mathrm{i}^2 + \tau_\mathrm{i}^2 - p_\mathrm{w}^2)}. \tag{B10}$$

Inserting the above derived parameters into the following equations from Hild for τ_r and p_r [39]

$$\tau_\mathrm{r} = (1 - g)\tau_\mathrm{i}\frac{I_\mathrm{r}}{I_\mathrm{i}}, \tag{B11}$$

$$p_\mathrm{r} = g \cdot I_\mathrm{r} + (1 - g) \cdot p_\mathrm{i}\frac{I_\mathrm{r}}{I_\mathrm{i}}, \tag{B12}$$

the tangential and normal momentum carried away from the wall by the particle can be described using the parameters α_T and g:

$$\tau_\mathrm{r} = (1 - g)\tau_\mathrm{i} \cdot \sqrt{\frac{p_\mathrm{i}^2 + \tau_\mathrm{i}^2 - \alpha_\mathrm{T}(p_\mathrm{i}^2 + \tau_\mathrm{i}^2 - p_\mathrm{w}^2)}{p_\mathrm{i}^2 + \tau_\mathrm{i}^2}}, \tag{B13}$$

$$p_\mathrm{r} = \sqrt{p_\mathrm{i}^2 + \tau_\mathrm{i}^2 - \alpha_\mathrm{T}(p_\mathrm{i}^2 + \tau_\mathrm{i}^2 - p_\mathrm{w}^2)} \cdot \left(g + (1 - g)\frac{p_\mathrm{i}}{\sqrt{p_\mathrm{i}^2 + \tau_\mathrm{i}^2}} \right), \tag{B14}$$

and thus, α_n and σ_t can be obtained utilizing Eq. 8 and Eq. B3 for given α_T and g. However, it should be noted that τ_i, p_i and p_w are determined using Sentman's equation in a 2D simplified version, which is valid for one area element with a given orientation regarding the velocity vector. Hence, the values for τ_i, p_i and p_w as well as τ_r and p_r change with different orientation of the considered area element. Assuming a constant energy and momentum accommodation over the satellite, the respective parameters may still be used on one representative area element to derive the normal energy accommodation coefficient and tangential momentum accommodation coefficient.

The derived input parameters for the use of the CLL model according to the given α_T can be found in Table 7 and were used for all the CLL ADBSat calculations within this article.

Funding Open Access funding enabled and organized by Projekt DEAL.

Data availability statement The data that support the findings of this study are available from the corresponding author upon reasonable request.

Declarations

Conflict of interest The authors have no conflict of interest to declare that are relevant to the content of this article.

References

1. Crisp, N.H., Roberts, P.C.E., Livadiotti, S., Oiko, V.T.A., Edmondson, S., Haigh, S.J., Huyton, C., Sinpetru, L.A., Smith, K.L., Worrall, S.D., Becedas, J., Domínguez, R.M., González, D., Hanessian, V., Mølgaard, A., Nielsen, J., Bisgaard, M., Chan, Y.-A., Fasoulas, S., Herdrich, G.H., Romano, F., Traub, C., Garcia-Almiñana, D., Rodriguez-Donaire, S., Sureda, M., Kataria, D., Outlaw, R., Belkouchi, B., Conte, A., Perez, J.S., Villain, R., Heißerer, B., Schwalber, A.: The benefits of very low earth orbit for earth observation missions. Prog. Aerosp. Sci. **117**, 100619 (2020). https://doi.org/10.1016/j.paerosci.2020.100619
2. D'Amico, S.: Autonomous formation flying in low earth orbit. PhD thesis, Delft University of Technology (2010)
3. Leonard, C.L., Hollister, W., Bergmann, E.: Orbital formationkeeping with differential drag. J. Guid. Control. Dyn. **12**(1), 108–113 (1987). https://doi.org/10.2514/3.20374
4. Bevilacqua, R., Romano, M.: Rendezvous maneuvers of multiple spacecraft using differential drag under j2 perturbation. J. Guid. Control. Dyn. **31**(6), 1595–1607 (2008). https://doi.org/10.2514/1.36362
5. Pérez, D., Bevilacqua, R.: Differential drag spacecraft rendezvous using an adaptive lyapunov control strategy. Acta Astronaut. **83**, 196–207 (2012). https://doi.org/10.1016/j.actaastro.2012.09.005
6. Dell'Elce, L., Kerschen, G.: Optimal propellantless rendez-vous using differential drag. Acta Astronaut. **109**, 112–123 (2015). https://doi.org/10.1016/j.actaastro.2015.01.011
7. Dell'Elce, L.: Satellite orbits in the atmosphere. PhD thesis (2015)
8. Ivanov, D., Monakhova, U., Guerman, A., Ovchinnikov, M.: Decentralized control of nanosatellite tetrahedral formation flying using aerodynamic forces. Aerospace **8**(8), 199 (2021). https://doi.org/10.3390/aerospace8080199
9. Ivanov, D., Monakhova, U., Guerman, A., Ovchinnikov, M., Roldugin, D.: Decentralized differential drag based control of nanosatellites swarm spatial distribution using magnetorquers. Adv. Space Res. **67**(11), 3489–3503 (2021). https://doi.org/10.1016/j.asr.2020.05.024
10. Lewin, A.W.: Low-cost operation of the orbcomm satellite constellation. J. Reduc. Space Mission Cost **1**(1), 105–117 (1998). https://doi.org/10.1023/A:1009987231306
11. Foster, C., Mason, J., Vittaldev, V., Leung, L., Beukelaers, V., Stepan, L., Zimmerman, R.: Constellation phasing with differential drag on planet labs satellites. J. Spacecr. Rocket. **20**(5), 1–11 (2017). https://doi.org/10.2514/1.A33927
12. Gangestad, J.W., Hardy, B.S., Hinkley, D.A.: Operations, orbit determination, and formation control of the aerocube-4 cubesats. In: 27th Annual AIAA/USU Conference on Small Satellites (2013)
13. Yoon, Z., Lim, Y., Grau, S., Frese, W., Garcia, M.A.: Orbit deployment and drag control strategy for formation flight while minimizing collision probability and drift. CEAS Space J. **12**(3), 397–410 (2020). https://doi.org/10.1007/s12567-020-00308-6
14. Ben-Yaacov, O., Gurfil, P.: Stability and performance of orbital elements feedback for cluster keeping using differential drag. J. Astronaut. Sci. **61**(2), 198–226 (2014). https://doi.org/10.1007/s40295-014-0022-0
15. Horsley, M., Nikolaev, S., Pertica, A.: Small satellite rendezvous using differential lift and drag. J. Guid. Control. Dyn. **36**(2), 445–453 (2013). https://doi.org/10.2514/1.57327
16. Smith, B., Boyce, R., Brown, L., Garratt, M.: Investigation into the practicability of differential lift-based spacecraft rendezvous. J. Guid. Control. Dyn. **40**(10), 2682–2689 (2017). https://doi.org/10.2514/1.G002537
17. Smith, B.: A comprehensive examination of low earth orbit aerodynamic accelerations for satellite formation control. PhD thesis (2019)
18. Hu, Y., Lu, Z., Liao, W., Zhang, X.: Differential aerodynamic force-based formation control of nanosatellites using yaw angle deviation. J. Guid. Control. Dyn. **44**(12), 1–15 (2021). https://doi.org/10.2514/1.G006141
19. Virgili-Llop, J., Roberts, P.C.E., Palmer, K., Hobbs, S., Kingston, J.: Descending sun-synchronous orbits with aerodynamic inclination correction. J. Guid. Control. Dyn. **38**(5), 831–842 (2015). https://doi.org/10.2514/1.G000183
20. Traub, C., Romano, F., Binder, T., Boxberger, A., Herdrich, G.H., Fasoulas, S., Roberts, P.C.E., Smith, K., Edmondson, S., Haigh, S., et al.: On the exploitation of differential aerodynamic lift and drag as a means to control satellite formation flight. CEAS Space J. **12**, 15–32 (2020). https://doi.org/10.1007/s12567-019-00254-y
21. Traub, C., Herdrich, G.H., Fasoulas, S.: Influence of energy accommodation on a robust spacecraft rendezvous maneuver using differential aerodynamic forces. CEAS Space J. **12**, 43–63 (2020). https://doi.org/10.1007/s12567-019-00258-8
22. Traub, C., Fasoulas, S., Herdrich, G.H.: A planning tool for optimal three-dimensional formation flight maneuvers of satellites in vleo using aerodynamic lift and drag via yaw angle deviations. Acta Astronaut. **198**, 135–151 (2022). https://doi.org/10.1016/j.actaastro.2022.04.010

23. Traub, C.: Differential aerodynamic forces as a means to control satellite formation flight. PhD thesis (2023). https://doi.org/10.18419/opus-13281
24. Hild, F., Traub, C., Pfeiffer, M., Beyer, J., Fasoulas, S.: Optimisation of satellite geometries in very low earth orbits for drag minimisation and lifetime extension. Acta Astronaut. **201**, 340–352 (2022). https://doi.org/10.1016/j.actaastro.2022.09.032
25. Walsh, J.A., Berthoud, L.: Reducing spacecraft drag in very low earth orbit through shape optimisation. 7th European Conference for Aeronautics and Aerospace Sciences (2017) https://doi.org/10.13009/EUCASS2017-449
26. Walter, U.: Astronautics: The physics of spaceflight. Third edition edn. (2018). https://doi.org/10.1007/978-3-319-74373-8
27. Sentman, L.H.: Free molecule flow theory and its application to the determination of aerodynamic forces: Technical Report, (1961). https://apps.dtic.mil/sti/citations/ad0265409
28. Chambre, P.A., Schaaf, S.A.: Flow of Rarefied Gases. Princeton University Press, Princeton (1958)
29. Walker, P.A.: Mehta, Koller,: Drag coefficient model using the cercignani-lampis-lord gas-surface interaction model. J. Spacecr. Rocket. **51**(5), 1544–1563 (2014). https://doi.org/10.2514/1.A32677
30. Picone, J.M., Hedin, A.E., Drob, D.P., Aikin, A.C.: Nrlmsise-00 empirical model of the atmosphere: statistical comparisons and scientific issues. J. Geophys. Res. Space Phys. **107**(A12), 15–11516 (2002). https://doi.org/10.1029/2002JA009430
31. Doornbos, E.: Thermospheric Density and Wind Determination from Satellite Dynamics. Springer Theses. Springer, Berlin Heidelberg, Berlin, Heidelberg (2012)
32. Llop, J.V.: Spacecraft flight in the atmosphere. PhD thesis, Cranfield University (2014)
33. Livadiotti, S., Crisp, N.H., Roberts, P.C.E., Oiko, V.T.A., Christensen, S., Dominguez, R.M., Herdrich, G.H.: Uncertainties and design of active aerodynamic attitude control in very low earth orbit. J. Guid. Control. Dyn. **45**(5), 859–874 (2022)
34. Heidt, H., Puig-Suari, J., Moore, A., Nakasuka, S., Twiggs, R.: Cubesat: A new generation of picosatellite for education and industry low-cost space experimentation. Proceedings of the Small Satellite Conference **Technical Session V: Lessons Learned - In Success and Failure**(SSC00-V-5) (2000)
35. Pilinski, M.D., Argrow, B.M., Palo, S.E.: Semiempirical model for satellite energy-accommodation coefficients. J. Spacecr. Rocket. **47**(6), 951–956 (2010). https://doi.org/10.2514/1.49330
36. Sinpetru, L.A., Crisp, N.H., Mostaza-Prieto, D., Livadiotti, S., Roberts, P.C.E.: Adbsat: methodology of a novel panel method tool for aerodynamic analysis of satellites. Comput. Phys. Commun. **275**, 108326 (2022). https://doi.org/10.1016/j.cpc.2022.108326
37. Fasoulas, S., Munz, C.-D., Pfeiffer, M., Beyer, J., Binder, T., Copplestone, S., Mirza, A., Nizenkov, P., Ortwein, P., Reschke, W.: Combining particle-in-cell and direct simulation monte carlo for the simulation of reactive plasma flows. Phys. Fluids **31**(7), 072006 (2019). https://doi.org/10.1063/1.5097638
38. Bird, G.A.: Molecular gas dynamics and the direct simulation of gas flows, Repr edn. Oxford science publications, vol. 42. Clarendon Press, Oxford (1994)
39. Hild, F.: Adaptation and application of piclas for the design of vleo satellite geometries. Master thesis, University of Stuttgart (2021)
40. Roberts, P.C.E., Crisp, N.H., Edmondson, S., Haigh, S.J., Holmes, B.E.A., Livadiotti, S., Macario-Rojas, A., Oiko, V.T.A., Smith, K.L., Sinpetru, L.A., Becedas, J., Domínguez, R.M., Sulliotti-Linner, V., Christensen, S., Jensen, T.K., Nielsen, J., Bisgaard, M., Chan, Y.-A., Herdrich, G.H., Romano, F., Fasoulas, F., Traub, C., Garcia-Almiñana, D., Garcia-Berenguer, M., Rodriguez-Donaire, S., Sureda, M., Kataria, D., Belkouchi, B., Conte, A., Seminari, S., Villain, R., Schwalber, A.: Discoverer: Developing technologies to enable commercial satellite operations in very low earth orbit. In: 71st International Astronautical Congress (IAC) - The Cyber Edition (2020)
41. Sinpetru, L.A., Crisp, N.H., Roberts, P.C.E., Sulliotti-Linner, V., Hanessian, V., Herdrich, G.H., Romano, F., Garcia-Almiñana, D., Rodríguez-Donaire, S., Seminari, S.: Adbsat: Verification and validation of a novel panel method for quick aerodynamic analysis of satellites. Comput. Phys. Commun. **275**, 108327 (2022)